

Article

# In Situ Observations Reveal the Five-fold Twin-Involved Growth of Gold Nanorods by Particle Attachment

Qi Sun <sup>1,2,†</sup>, Loukya Boddapati <sup>3,†</sup> , Linan Wang <sup>2</sup>, Junjie Li <sup>2,4,\*</sup>  and Francis Leonard Deepak <sup>3,\*</sup><sup>1</sup> School of Semiconductor Science and Technology, South China Normal University, Foshan 528225, China<sup>2</sup> Research Center for Crystal Materials, CAS Key Laboratory of Functional Materials and Devices for Special Environments, Xinjiang Technical Institute of Physics & Chemistry, CAS, Urumqi 830011, China<sup>3</sup> Nanostructured Materials Group, International Iberian Nanotechnology Laboratory (INL), Avenida Mestre Jose Veiga, 4715-330 Braga, Portugal<sup>4</sup> Center of Materials Science and Optoelectronics Engineering, University of Chinese Academy of Sciences, Beijing 100049, China

\* Correspondence: lijunjie@ms.xjb.ac.cn (J.L.); leonard.francis@inl.int (F.L.D.)

† These authors contributed equally to this work.

**Abstract:** Crystallization plays a critical role in determining crystal size, purity and morphology. Therefore, uncovering the growth dynamics of nanoparticles (NPs) atomically is important for the controllable fabrication of nanocrystals with desired geometry and properties. Herein, we conducted in situ atomic-scale observations on the growth of Au nanorods (NRs) by particle attachment within an aberration-corrected transmission electron microscope (AC-TEM). The results show that the attachment of spherical colloidal Au NPs with a size of about 10 nm involves the formation and growth of neck-like (NL) structures, followed by five-fold twin intermediate states and total atomic rearrangement. The statistical analyses show that the length and diameter of Au NRs can be well regulated by the number of tip-to-tip Au NPs and the size of colloidal Au NPs, respectively. The results highlight five-fold twin-involved particle attachment in spherical Au NPs with a size of 3–14 nm, and provide insights into the fabrication of Au NRs using irradiation chemistry.

**Keywords:** in situ observation; Au nanorod; crystal growth; particle attachment; transmission electron microscopy



**Citation:** Sun, Q.; Boddapati, L.; Wang, L.; Li, J.; Deepak, F.L. In Situ Observations Reveal the Five-fold Twin-Involved Growth of Gold Nanorods by Particle Attachment. *Nanomaterials* **2023**, *13*, 796. <https://doi.org/10.3390/nano13050796>

Academic Editor: James Evans

Received: 27 December 2022

Revised: 31 January 2023

Accepted: 14 February 2023

Published: 21 February 2023



**Copyright:** © 2023 by the authors. Licensee MDPI, Basel, Switzerland. This article is an open access article distributed under the terms and conditions of the Creative Commons Attribution (CC BY) license (<https://creativecommons.org/licenses/by/4.0/>).

## 1. Introduction

Geometrical structure and chemical composition are the two important parameters that have a critical influence on the properties of functional materials [1–4]. NPs with zero-/one-/two-dimensional (0D/1D/2D) structures have received considerable attention in recent decades, and the fabrication of all kinds of nanostructures has been of central interest in this field [5–17]. Gold (Au) NPs, as one of the promising candidates for catalytic, electronic, plasmonic, molecular diagnostic and sensing applications, are well known for their tailorable size and surface chemistry, high stability and good biocompatibility [18–23]. In 1857, Faraday reported the synthesis of colloidal Au NPs for the first time [24]. Thereafter, a large number of experiments have been carried out to fabricate Au NPs with controllable size and unique morphology, involving various routes such as wet chemical synthesis at room temperature, hydrothermal processes, template methods and irradiation-assisted routes, all of which have been developed (for the synthesis of Au NPs) over recent decades [25,26]. Meanwhile, in order to clarify the crystal growth mechanism and thus achieve controllable chemical synthesis of Au NPs, the crystal growth dynamics of Au NPs have been investigated by ex situ and/or in situ observation techniques such as X-ray scattering (XRS) techniques, UV-VIS spectroscopy, X-ray absorption fine structure (XAFS) spectroscopy, atomic force microscopy (AFM), scanning electron microscopy (SEM), transmission electron microscopy (TEM), scanning TEM (STEM) and so on [21,27–31]. Among them, microscopies, especially

liquid cell TEM (LCTEM), have been regarded as a powerful tool to visualize crystal growth kinetics at the nano- or atomic-scale [32–34].

Based on classical crystal growth models, crystals are grown by simple structure replication, which does not involve structural transition or intermediate states. However, the classical mechanism or model cannot explain all of the phenomena that have recently been discovered in many crystallization processes. Ex situ and in situ studies have uncovered the existence of nonclassical crystal growth processes, including intraparticle growth [35,36], oriented attachment (OA) growth [37], grain boundary migration and surface-atom-migration dominated coalescence and growth pathways [38,39]. For examples, Tang et al. investigated the growth of Au NPs in 10.0 mM HAuCl<sub>4</sub> solutions by in situ LCTEM [40]. The formation of “cluster-cloud” (condensed atomic clusters) was observed in the crystallization, which plays a critical role in the formation of the initial crystal nucleus and crystal growth [40]. To illustrate the formation of a superlattice, Chen and Luijten et al. investigated the growth of Au superlattices from Au nanoprisms by in situ LCTEM in combination with Monte Carlo simulations [41]. To clarify the influence of ligands, the ligand-controlled OA processes were studied by Sun et al. in a LCTEM at the atomic scale [42]. To detect the substrate-effected coalescence growth, the coalescence process of Au NPs on crystalline (MgO) and amorphous (carbon) supports were studied by Li and Deepak et al. [21,23]. The results demonstrate that, compared to the amorphous carbon substrate, the crystalline MgO support is suitable for the migration of Au NPs/atoms, giving rise to rapid crystal growth kinetics. To uncover the influence of concentration, Kim et al. investigated the formation of spiky Au NPs from HAuCl<sub>4</sub> solutions with a broad solution concentration range by combining UV-vis spectra and in situ TEM, demonstrating the HAuCl<sub>4</sub> concentration-dependent crystal growth processes [43]. More recently, Li et al. uncovered the formation of Au NPs with a five-fold twinned structure by in situ TEM in combination with molecular dynamic simulations at the atomic scale [44]. The in situ dynamic observations provide nano- or atomic-scale information towards understanding the classical or non-classical crystal growth processes. Nevertheless, most of the in situ dynamic investigations were focused on the growth of Au NPs with a length/diameter aspect ratio of ~1, and studies on the growth of 1D Au NRs or NWs were quite limited [45–47].

In this work, we report in situ atomic-scale dynamic observations on the growth of Au NRs in an aberration-corrected TEM (ACTEM). To obtain atomic-scale resolution, highly dispersed Au NPs ~10 nm were employed for the in situ experiments. The results show that the Au NRs with length/diameter aspect ratios of ~1–3 are formed by the particle attachment mechanism under electron irradiation. At the initial stage, the Au NPs are connected with each other in a tip-to-tip way to construct the NL structures, which is different to the formation of a super-lattice by the direct particle attachment of cubic NPs. Subsequently, the formed NL structures show linear growth dynamics to achieve closed height and width with the adjacent NPs. Finally, the Au NPs display a total atomic rearrangement to construct a Au NR with low surface energy. It is worth noting that the five-fold twin structures are involved in the atomic arrangement process because of their low formation energy in the Au NPs with the size of ~3 to 14 nm. Moreover, the statistical analyses indicate that the length of the Au NRs can be easily controlled by the number of attached Au NPs, and their diameter is mainly dependent on the size of the attached Au NPs.

## 2. Experimental Section

### 2.1. Sample Preparation and Characterization

The highly dispersed citrate-capped Au NPs (size: 6 nm to 10 nm) in H<sub>2</sub>O were obtained from BBI Solutions Co., Ltd. Wales, UK (Gold Colloid (bbisolutions.com), 30 June 2020). To avoid possible aggregation, the colloidal Au NPs were stored in the original solution and used without further purification. Before utilization, the Au samples were diluted and dispersed by ultrasonication, and a few drops of this dispersion of Au solution

were dropped onto a carbon grid and then dried for structural characterizations and in situ TEM observations.

### 2.2. In situ TEM Observations

TEM imaging was carried out at 200 kV using a Titan Themis TEM equipped with both an image Cs corrector and probe Cs corrector, which provided an opportunity to probe the dynamic process under sub-angstrom resolution [19,48–50]. The images or videos were acquired using Tecnai Imaging and Analysis (TIA) software. The electron dose rates were controlled by the spot size.

## 3. Results and Discussion

To reduce the influence of size, the commercial Au NPs with a diameter of  $\sim 10$  nm were used for the dynamic observations. Before the experiments, the colloidal Au samples were dispersed by ultrasonication. Figure 1a shows the sphere-like morphology of the Au NPs used. Based on the statistical analyses on the diameter of 22 Au NPs in different regions in different TEM images, it can be seen that the colloidal Au NPs show a size distribution from 6 nm to 11 nm, and the averaged size is about 9 nm, as shown in Figure 1b. To confirm the crystal structure, high-resolution TEM images were acquired. Figure 1c shows a high resolution TEM image of a Au NP, and Figure 1d is the corresponding Fourier transformation (FFT) analysis. The results indicate the face-centered cubic structure in the colloidal Au NPs.

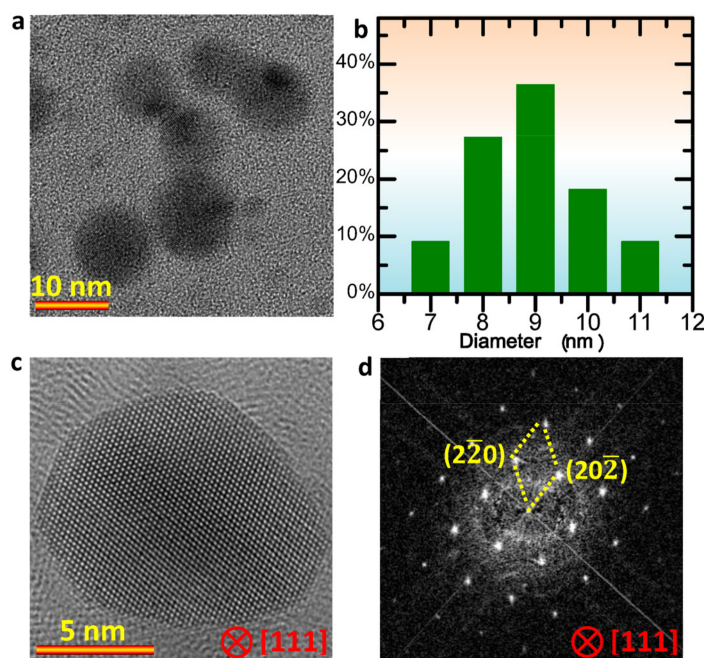


**Figure 1.** The morphology and size of Au NPs. (a) TEM image showing the morphology of Au NPs; (b) statistical analysis showing the size distribution of the highly dispersed Au NPs; (c,d) high-resolution TEM image and corresponding FFT pattern of a Au NP.

To probe the growth dynamic process of Au NRs, both STEM and TEM modes were employed, as shown in Figure 2. In Figure 2a–c, the sequential high-angle annular dark field (HAADF)-STEM images show that the Au NR can be grown by a particle attachment mechanism. However, in contrast with the direct particle attachment of cubic NPs in the formation of super-lattices of MOF, the spherical NP attachment involved the coalescence of a round-like grain boundary and total atomic rearrangement to minimize the surface energy and total energy. As shown in Figure 2b, a NL structure was formed at the initial stage. Subsequently, the NL structure grew to form a dumbbell-like structure (Figure 2c). Due to the disturbance of the scanning electron probe on the surface structure, as well as the

carbon contamination that starts to build-up during in situ observations, it was challenging to obtain high-quality videos under the HAADF-STEM mode.

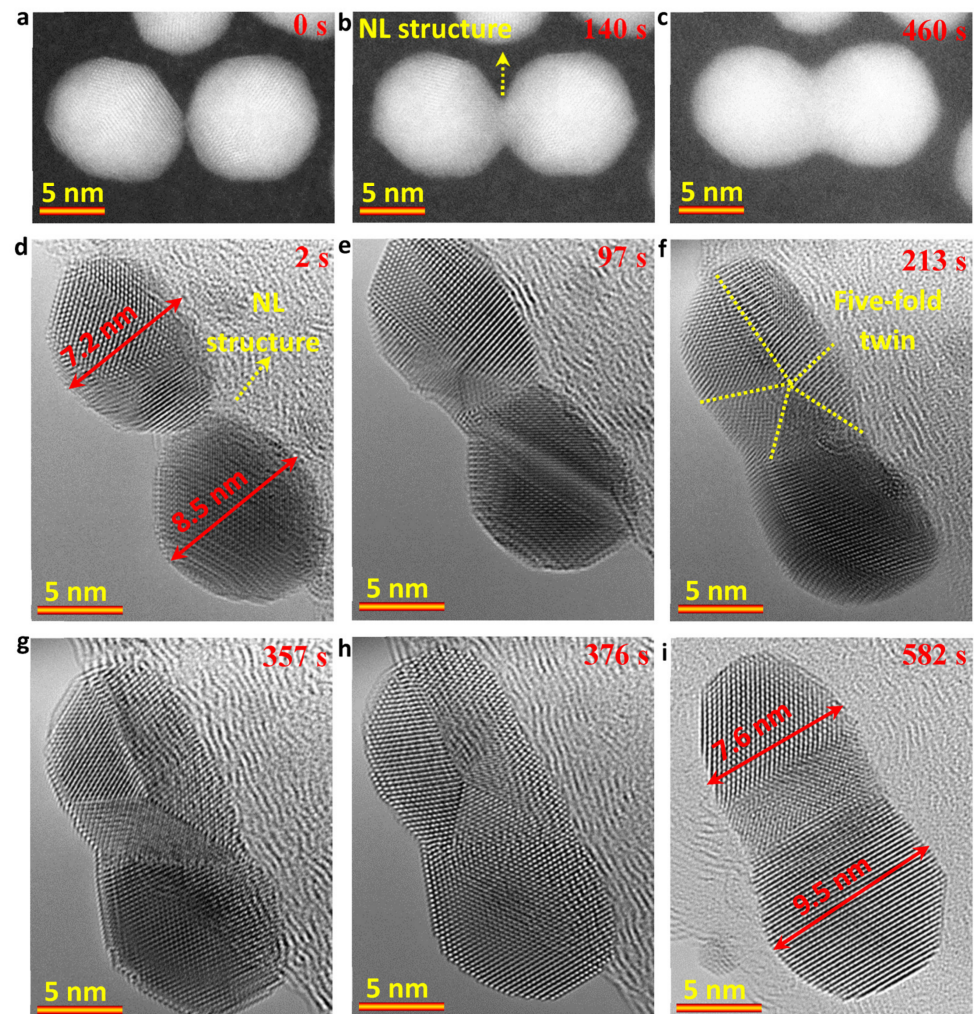


**Figure 2.** (a–c) Sequential HAADF-STEM images showing the growth of Au NRs with a length of  $\sim 20$  nm from two Au NPs; (d–i) Sequential TEM images from Video S1 showing the growth of Au NRs with a length of  $\sim 18$  nm at atomic scale by the attachment of two Au NPs. The electron dose rate is  $\sim 1.0 \times 10^5$  e/ $\text{\AA}^2$ s.

The attachment of two Au NPs (7.2 nm and 8.5 nm) were further recorded in TEM mode under an electron dose rate of  $1.0 \times 10^5$  e/ $\text{\AA}^2$ s. Figure 2d–i show the sequential atomic scale TEM results, which were obtained from Video S1. Similar to the HAADF-STEM results, the NL structure (Figure 2d) was further confirmed under TEM mode. Thereafter, the two Au NPs showed total atomic rearrangement, in which the five-fold twin structures were involved, as shown in Figure 2e–h and Video S1. The five-fold twin structure in the upper Au NP appeared at the initial contacting stage of the two Au NPs (Figure 2d–e). Thereafter, under the drive of minimizing the surface energy and total energy, the upper five-fold twin structure and the lower Au nanocrystal (Figure 2h) showed a total atomic rearrangement to achieve a closed or a same orientation (ideally) by forming smooth surface and reducing the interior defects like the twin boundaries in the NR. Moreover, the formed five-fold twin structure could be related to the size effect. Based on the thermodynamic analyses, the five-fold twin structure of Au NPs is thermodynamically stable with the size of 3 to 14 nm [44,51–53]. When the size of Au NP is larger than 14 nm, the five-fold twin structure disappears, as shown in Figure 2i. At 582 s, the mean diameter for the formed Au NR was measured to be  $\sim 8.5$  nm and the ratio of length/diameter was about 2.1.

To further check the growth dynamics of the NL structure, the change of the “neck” diameter along with time was investigated. Based on the sequential high-resolution TEM images in Video S1, the statistical analyses were carried out, and the results indicated a linear growth dynamic for the NL structure, as shown in Figure 3, which should be related to the atomic migration rate.

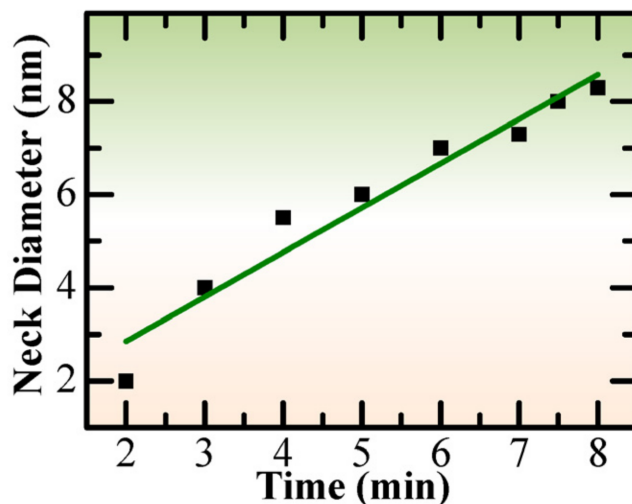


**Figure 3.** Statistical analysis showing the linear growth of neck diameter with time in Video S1.

The schematic diagram shown below (Figure 4) illustrates the attachment of spherical Au NPs with a size of 3 to 14 nm. As shown in Figure 4, the separated Au NPs first connected with each other to form an NL structure, and then showed a linear growth and total atomic rearrangement involving the formation and disappearance of the five-fold twin structure. Driven by minimizing the surface energy and total energy, the Au NR could be formed.

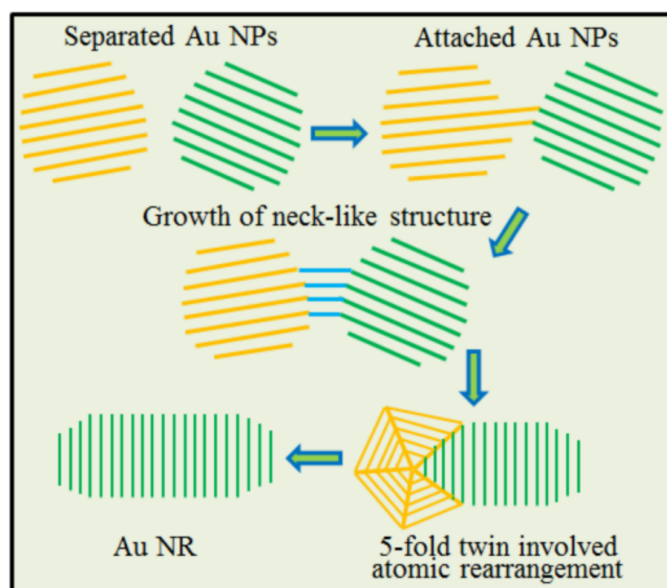


**Figure 4.** Schematic diagram showing the formation of Au NR by the attachment of Au NPs with a size of ~10 nm.

To detect the length-dependent-growth dynamics, three and four Au NP attachment (in a tip-to-tip way)-driven crystal growth of Au NRs were carried out, respectively. Figure 5a–f (Video S2) show the formation of a Au NR (Figure 5f) with a length of ~19 nm

by grouping three Au NPs (~8.9 nm, ~9.4 nm and ~8.4 nm) under an electron dose rate of  $\sim 1.0 \times 10^5 \text{ e}/\text{\AA}^2\text{s}$ . Figure 5g–l (Video S3) show the formation of a Au NR (Figure 5l) with a length of ~32.5 nm by attaching four Au NPs (~9.8 nm, ~9.0 nm, ~8.1 nm and ~9.8 nm) in a tip-to-tip way under an electron dose rate of  $\sim 1.0 \times 10^5 \text{ e}/\text{\AA}^2\text{s}$ . Similar to the attachment of two Au NPs in Figure 2, the attachment of three/four spherical Au NPs also shows the NL structures when the Au NPs are initially contacted with each other, and then follows a total atomic rearrangement and grain boundary migration to achieve a rod-like geometry from the bead-like structures. The diameters for the two NRs were 8.4 nm (Figure 5f) and 8.2 nm (averaged value in Figure 5l), and the length/diameter were ~2.3 (Figure 5f) and ~3.8 (Figure 5l), respectively. It means that the length is dependent on the number of attached Au NPs. Moreover, the thermodynamically stable five-fold twin structure in the small Au NPs with a size between 3 to 14 nm was also observed in both in situ dynamic observations (Videos S2 and S3).

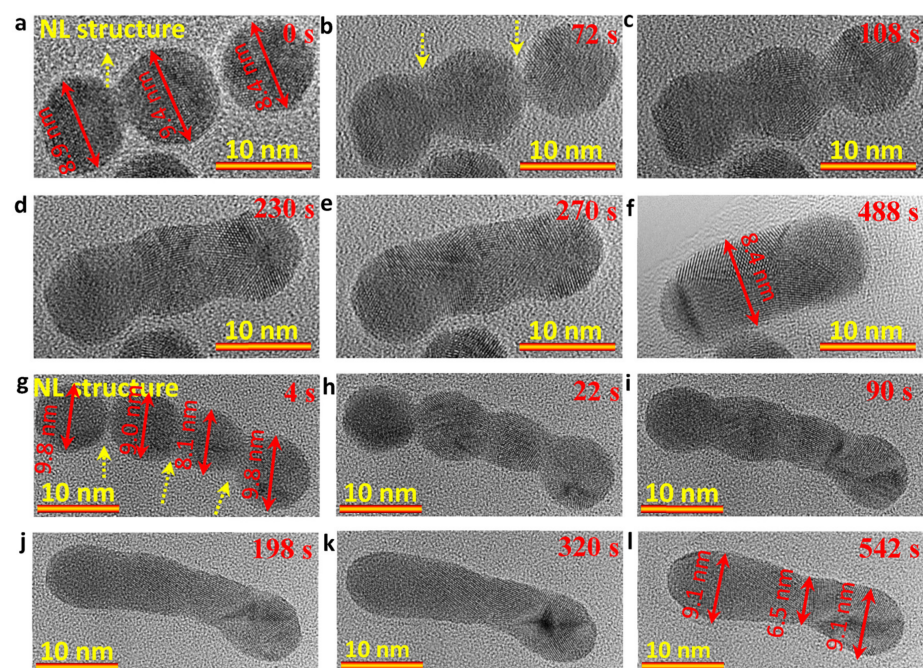


**Figure 5.** (a–f) Sequential TEM images from Video S2 showing the growth of Au NRs with a length of ~19 nm through the attachment of three Au NPs in a tip-to-tip way; (g–l) Sequential TEM images from Video S3 showing the growth of Au NRs with a length of ~32.5 nm through the attachment of four Au NPs in a tip-to-tip way. The electron dose rate is  $\sim 1.0 \times 10^5 \text{ e}/\text{\AA}^2\text{s}$ .

To shed further light on the structural evolution and to quantify the growth dynamics of the Au NRs with different lengths in Videos S1–S3, the change of length ( $l$ ), diameter ( $d$ ) and length–diameter ratio ( $l/d$ ) with time were investigated by statistical analyses. It is worth noting that the diameter  $d$  is an average value here. The results show that the length of the NPs is reduced with time (Figure 6a–c), and the diameter is related to the size of spherical Au NPs and time (Figure 6d–f). At the initial stage, the values of length and averaged width fluctuated rapidly, which can be attributed to the formation and growth of NL structures. The aspect (length/diameter) ratios (Figure 6g–i) indicate that the length of the Au NR formed via particle attachment is mainly determined by the number of tip-to-tip Au NPs, and the aspect (length/diameter) ratio can be modified by regulating the attachment time.

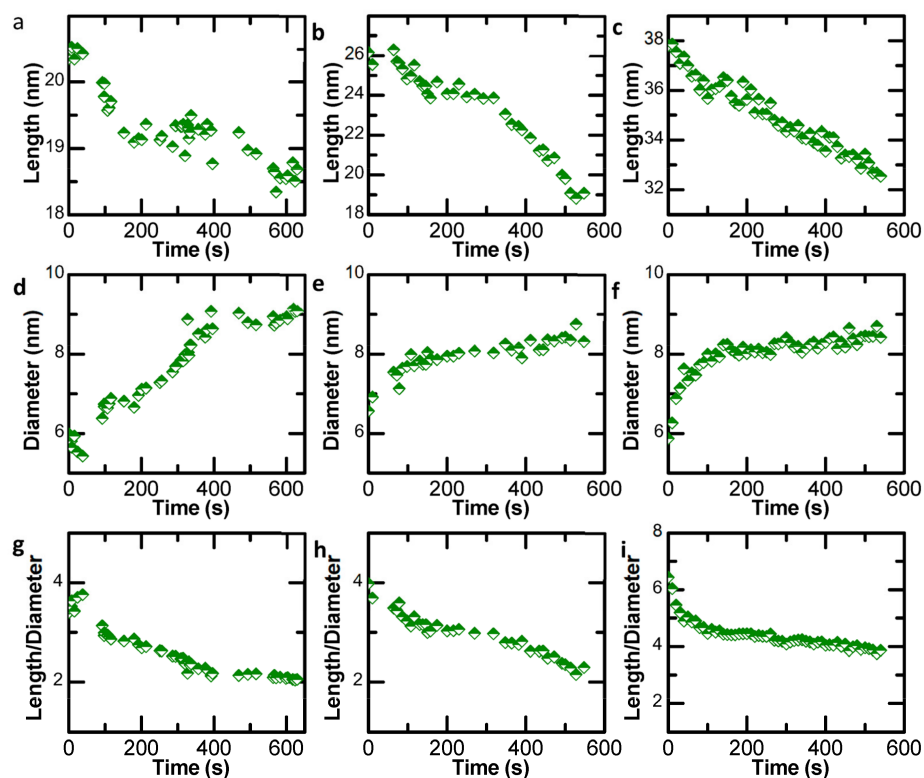


**Figure 6.** Statistical analyses showing the fluctuation of length (a–c), diameter (d–f) and aspect (length/diameter) ratio (g–i) of Au NRs along with time in Videos S1–S3. The Videos in supplementary information (SI) were played at seven times that of normal speed.

#### 4. Conclusions

The in situ atomic-scale observations on the formation of Au NRs by spherical colloidal Au NPs represents a significant step forward in understanding the growth mechanisms of NRs using spherical particle attachment. The experimental results show that the attachment of spherical Au NPs includes the formation and growth of NL structures and the atomic rearrangement involves the formation of five-fold twin structures in Au NPs with a size of ~3 to 14 nm. Moreover, the statistical analyses indicate that the formed NL structure displayed linear growth dynamics. The length of Au NRs can be well regulated by the number of tip-to-tip Au NPs, and the diameters are mainly determined by the size of spherical Au NPs. These findings indicate that the attachment of spherical NPs during the growth of Au NRs could be different to the attachment of cubic NPs in the formation of a super-lattice, and provide new insights into the fabrication of Au NRs based on colloidal Au NPs and irradiation chemistry.

**Supplementary Materials:** The following supporting information can be downloaded at: <https://www.mdpi.com/article/10.3390/nano13050796/s1>, Video S1: The growth of Au NR from two NPs; Video S2: The growth of Au NR from three NPs; Video S3: The growth of Au NR from four NPs.

**Author Contributions:** Conceptualization, F.L.D. and L.B.; methodology and data analysis, L.B. and Q.S.; writing, Q.S., L.W., J.L. and F.L.D.; supervision, J.L. and F.L.D.; funding acquisition, J.L. and F.L.D. All authors have read and agreed to the published version of the manuscript.

**Funding:** This work was supported by the High-level Talent Project of Xinjiang Uygur Autonomous Region (2020000039), the National Natural Science Foundation of China (52002398) and the Xinjiang Key Laboratory of Electronic Information Materials and Devices (2017D04029).

**Data Availability Statement:** The data presented in this study are available on request from the corresponding author.

**Conflicts of Interest:** The authors declare no competing financial interests.

## References

1. Crawley, J.W.M.; Gow, I.E.; Lawes, N.; Kowalec, I.; Kabalan, L.; Catlow, C.R.A.; Logsdail, A.J.; Taylor, S.H.; Dummer, N.F.; Hutchings, G.J. Heterogeneous trimetallic nanoparticles as catalysts. *Chem. Rev.* **2022**, *122*, 6795–6849. [[CrossRef](#)] [[PubMed](#)]
2. Mutailipu, M.; Poeppelmeier, K.R.; Pan, S. Borates: A rich source for optical materials. *Chem. Rev.* **2021**, *121*, 1130–1202. [[CrossRef](#)] [[PubMed](#)]
3. Aboyewa, J.A.; Sibuyi, N.R.S.; Goboza, M.; Murtz, L.A.; Oguntibeju, O.O.; Meyer, M. Co-treatment of Caco-2 cells with doxorubicin and gold nanoparticles produced from cyclopia intermedia extracts or mangiferin enhances drug effects. *Nanomaterials* **2022**, *12*, 3918. [[CrossRef](#)] [[PubMed](#)]
4. Abudurusuli, A.; Huang, J.; Wang, P.; Yang, Z.H.; Pan, S.; Li, J.J.  $\text{Li}_4\text{MgGe}_2\text{S}_7$ : The first alkali and alkaline-earth diamond-like infrared nonlinear optical material with exceptional large band gap. *Angew. Chem. Int. Ed.* **2021**, *60*, 24131–24136. [[CrossRef](#)] [[PubMed](#)]
5. Liu, J.W.; Huang, J.T.; Niu, W.X.; Tan, C.L.; Zhang, H. Unconventional-phase crystalline materials constructed from multiscale building blocks. *Chem. Rev.* **2021**, *121*, 5830–5888. [[CrossRef](#)]
6. Mondal, S.; Rajesh, T.; Dhar, B.B.; Snellman, M.; Li, J.; Francis, L.D.; Devi, R.N. Understanding alloy structure and composition in sinter-resistant  $\text{AgPd@SiO}_2$  encapsulated catalysts and their effect on catalytic properties. *New J. Chem.* **2017**, *41*, 14652–14658. [[CrossRef](#)]
7. Li, J.J.; Lian, Z.; Li, Q.; Wang, Z.C.; Liu, L.F.; Deepak, F.L.; Liu, Y.P.; Li, B.; Xu, J.Y.; Chen, Z.X. Boosting acidic water oxidation performance by constructing arrays-like nanoporous  $\text{Ir}_x\text{Ru}_{1-x}\text{O}_2$  with abundant atomic steps. *Nano Res.* **2022**, *15*, 5933–5939. [[CrossRef](#)]
8. Liu, D.Y.; Zeng, Q.; Hu, C.Q.; Chen, D.; Liu, H.; Han, Y.S.; Xu, L.; Zhang, Q.B.; Yang, J. Light doping of tungsten into copper-platinum nanoalloys for boosting their electrocatalytic performance in methanol oxidation. *Nano Res. Energy* **2022**, *1*, e9120017. [[CrossRef](#)]
9. Li, J.J.; Shen, J.; Li, Z.Q.; Li, X.D.; Sun, Z.; Hu, Z.G.; Huang, S.M. Wet chemical route to the synthesis of kesterite  $\text{Cu}_2\text{ZnSnS}_4$  nanocrystals and their applications in lithium ion batteries. *Mater. Lett.* **2013**, *92*, 330–333. [[CrossRef](#)]
10. Li, L.L.; Hasan, I.M.U.; Farwa, He, R.N.; Peng, L.W.; Xu, N.N.; Niazi, N.K.; Zhang, J.N.; Qiao, J.L. Copper as a single metal atom based photo-, electro-, and photoelectrochemical catalyst decorated on carbon nitride surface for efficient  $\text{CO}_2$  reduction: A review. *Nano Res. Energy* **2022**, *1*, e9120015. [[CrossRef](#)]
11. Xiong, D.H.; Zhang, Q.Q.; Li, W.; Li, J.J.; Fu, X.L.; Cerqueira, M.F.; Alpuim, P.; Liu, L.F. Atomic-layer-deposited ultrafine  $\text{MoS}_2$  nanocrystals on cobalt foam for efficient and stable electrochemical oxygen evolution. *Nanoscale* **2017**, *9*, 2711–2717. [[CrossRef](#)]
12. Gao, M.; Wang, Z.; Lek, D.G.; Wang, Q. Towards high power density aqueous redox flow batteries. *Nano Res. Energy* **2022**, *2*, e9120045. [[CrossRef](#)]
13. Xu, J.Y.; Liu, T.F.; Li, J.J.; Li, B.; Liu, Y.F.; Zhang, B.S.; Xiong, D.H.; Amorim, I.; Li, W.; Liu, L.F. Boosting the hydrogen evolution performance of ruthenium clusters through synergistic coupling with cobalt phosphide. *Energy Environ. Sci.* **2018**, *11*, 1819–1827. [[CrossRef](#)]
14. Xu, J.Y.; Liu, Y.F.; Li, J.J.; Amorim, I.; Zhang, B.S.; Xiong, D.H.; Zhang, N.; Thalluri, S.M.; Sousa, J.P.; Liu, L.F. Hollow cobalt phosphide octahedral pre-catalysts with exceptionally high intrinsic catalytic activity for electro-oxidation of water and methanol. *J. Mater. Chem. A* **2018**, *6*, 20646–20652. [[CrossRef](#)]
15. Li, J.J.; Deepak, F.L. In situ generation of sub-10 nm silver nanowires under electron beam irradiation in a TEM. *Chem. Commun.* **2020**, *56*, 4765–4768. [[CrossRef](#)] [[PubMed](#)]
16. Li, Q.; Wei, B.; Li, Y.; Xu, J.Y.; Li, J.J.; Liu, L.F.; Deepak, F.L. Large-scale fabrication of hollow  $\text{Pt}_3\text{Al}$  nanoboxes and their electrocatalytic performance for hydrogen evolution reaction. *ACS Sustain. Chem. Eng.* **2019**, *7*, 9842–9847. [[CrossRef](#)]
17. Guo, F.J.; Zhang, M.Y.; Yi, S.C.; Li, X.X.; Xin, R.; Yang, M.; Liu, B.; Chen, H.B.; Li, H.M.; Liu, Y.J. Metal-coordinated porous polydopamine nanospheres derived  $\text{Fe}_3\text{N-FeCo}$  encapsulated N-doped carbon as a highly efficient electrocatalyst for oxygen reduction reaction. *Nano Res. Energy* **2022**, *1*, e9120027. [[CrossRef](#)]
18. Zhou, T.X.; Huang, J.; Zhao, W.S.; Guo, R.; Cui, S.C.; Li, Y.Q.; Zhang, X.L.; Liu, Y.; Zhang, Q. Multifunctional plasmon-tunable Au nanostars and their applications in highly efficient photothermal inactivation and ultra-sensitive SERS detection. *Nanomaterials* **2022**, *12*, 4232. [[CrossRef](#)]
19. Li, J.J.; Wang, Z.C.; Chen, C.L.; Huang, S.M. Atomic-scale observation of migration and coalescence of Au nanoclusters on YSZ surface by aberration-corrected STEM. *Sci. Rep.* **2014**, *4*, 5521. [[CrossRef](#)]
20. Babich, E.; Reduto, I.; Lipovskii, A. Diffusive formation of Au/Ag alloy nanoparticles of governed composition in glass. *Nanomaterials* **2022**, *12*, 4202. [[CrossRef](#)]
21. Li, J.J.; Yin, D.Q.; Chen, C.L.; Li, Q.; Lin, L.Y.; Sun, R.; Huang, S.M.; Wang, Z.C. Atomic-scale observation of dynamical fluctuation and three-dimensional structure of gold clusters. *J. Appl. Phys.* **2015**, *117*, 085303. [[CrossRef](#)]

22. Volders, J.; Elen, K.; Raes, A.; Ninakanti, R.; Kelchtermans, A.-S.; Sastre, F.; Hardy, A.; Cool, P.; Verbruggen, S.W.; Buskens, P.; et al. Sunlight-powered reverse water gas shift reaction catalysed by plasmonic Au/TiO<sub>2</sub> nanocatalysts: Effects of Au particle size on the activity and selectivity. *Nanomaterials* **2022**, *12*, 4153. [[CrossRef](#)] [[PubMed](#)]
23. Li, Q.; Yin, D.Q.; Li, J.J.; Francis, L.D. Atomic-scale understanding of gold cluster growth on different substrates and adsorption-induced structural change. *J. Phys. Chem. C* **2017**, *122*, 1753–1760. [[CrossRef](#)]
24. Faraday, M.X. The bakerian lecture.—Experimental relations of gold (and other metals) to light. *Philos. Trans. R. Soc. Lond.* **1857**, *147*, 145–181. [[CrossRef](#)]
25. Stearns, L.A.; Chhabra, R.; Sharma, J.; Liu, Y.; Petuskey, W.; Yan, H.; Chaput, J.C. Template-directed nucleation and growth of inorganic nanoparticles on DNA scaffolds. *Angew. Chem. Int. Ed.* **2009**, *48*, 8494–8496. [[CrossRef](#)] [[PubMed](#)]
26. Yao, T.; Sun, Z.H.; Li, Y.Y.; Pan, Z.Y.; Wei, H.; Xie, Y.; Nomura, M.; Niwa, Y.; Yan, W.S.; Wu, Z.Y.; et al. Insights into initial kinetic nucleation of gold nanocrystals. *J. Am. Chem. Soc.* **2010**, *132*, 7696–7701. [[CrossRef](#)] [[PubMed](#)]
27. Li, J.J.; Deepak, F.L. In situ kinetic observations on crystal nucleation and growth. *Chem. Rev.* **2022**, *122*, 16911–16982. [[CrossRef](#)]
28. AbeCassis, B.; Testard, F.; Kong, Q.; Francois, B.; Spalla, O. Influence of monomer feeding on a fast gold nanoparticles synthesis: Time-resolved XANES and SAXS experiments. *Langmuir* **2010**, *26*, 13847–13854. [[CrossRef](#)]
29. Polte, J.; Erler, R.; Thunemann, A.F.; Sokolov, S.; Ahner, T.T.; Rademann, K.; Emmerling, F.; Kraehnert, R. Nucleation and growth of gold nanoparticles studied via in situ small angle X-ray scattering at millisecond time resolution. *ACS Nano* **2010**, *4*, 1076–1082. [[CrossRef](#)]
30. Ohyama, J.; Teramura, K.; Higuchi, Y.; Shishido, T.; Hitomi, Y.; Kato, K.; Tanida, H.; Uruga, T.; Tanaka, T. In situ observation of nucleation and growth process of gold nanoparticles by quick XAFS spectroscopy. *ChemPhysChem* **2011**, *12*, 127–131. [[CrossRef](#)]
31. Ishida, T.; Murayama, T.; Taketoshi, A.; Haruta, M. Importance of size and contact structure of gold nanoparticles for the genesis of unique catalytic processes. *Chem. Rev.* **2020**, *120*, 464–525. [[CrossRef](#)] [[PubMed](#)]
32. Li, J.J.; Li, Q.; Wang, Z.C.; Deepak, F.L. Real-time dynamical observation of lattice induced nucleation and growth in interfacial solid-solid phase transitions. *Cryst. Growth Des.* **2016**, *16*, 7256–7262. [[CrossRef](#)]
33. Li, J.J.; Wang, Z.C.; Deepak, F.L. Direct atomic-scale observation of intermediate pathways of melting and crystallization in supported Bi nanoparticles. *J. Phys. Chem. Lett.* **2018**, *9*, 961–969. [[CrossRef](#)] [[PubMed](#)]
34. Li, J.J.; Wang, Z.C.; Li, Y.P.; Deepak, F.L. In situ atomic-scale observation of kinetic pathways of sublimation in silver nanoparticles. *Adv. Sci.* **2019**, *6*, 1802131. [[CrossRef](#)] [[PubMed](#)]
35. Peng, Z.A.; Peng, X. Mechanisms of the shape evolution of CdSe nanocrystals. *J. Am. Chem. Soc.* **2001**, *123*, 1389–1395. [[CrossRef](#)]
36. Thanh, N.T.K.; Maclean, N.; Mahiddine, S. Mechanisms of nucleation and growth of nanoparticles in solution. *Chem. Rev.* **2014**, *114*, 7610–7630. [[CrossRef](#)] [[PubMed](#)]
37. Miot, J.; Etique, M. Formation and transformation of iron-bearing minerals by iron(II)-oxidizing and iron(III)-reducing bacteria. *Iron Oxides* **2016**, *11*, 243–268. [[CrossRef](#)]
38. Li, J.J.; Chen, J.C.; Wang, H.; Chen, N.; Wang, Z.C.; Guo, L.; Deepak, F.L. In situ atomic-scale study of particle-mediated nucleation and growth in amorphous bismuth to nanocrystal phase transformation. *Adv. Sci.* **2018**, *5*, 1700992. [[CrossRef](#)]
39. Li, J.J.; Li, Y.P.; Wang, Z.C.; Deepak, F.L. Atomic-scale dynamic observation reveals temperature-dependent multistep nucleation pathways in crystallization. *Nanoscale Horiz.* **2019**, *4*, 1302–1309. [[CrossRef](#)]
40. Jin, B.; Wang, Y.M.; Liu, Z.M.; France-Lanord, A.; Grossman, J.C.; Jin, C.H.; Tang, R.K. Revealing the cluster-cloud and its role in nanocrystallization. *Adv. Mater.* **2019**, *31*, 1808225. [[CrossRef](#)]
41. Ou, Z.H.; Wang, Z.W.; Luo, B.B.; Luijten, E.; Chen, Q. Kinetic pathways of crystallization at the nanoscale. *Nat. Mater.* **2020**, *19*, 450–455. [[CrossRef](#)] [[PubMed](#)]
42. Zhu, C.; Liang, S.X.; Song, E.H.; Zhou, Y.J.; Wang, W.; Shan, F.; Shi, Y.T.; Hao, C.; Yin, K.B.; Zhang, T.; et al. In-situ liquid cell transmission electron microscopy investigation on oriented attachment of gold nanoparticles. *Nat. Commun.* **2018**, *9*, 421. [[CrossRef](#)]
43. Jung, W.G.; Park, J.H.; Jo, Y.R.; Kim, B.J. Growth kinetics of individual Au spiky nanoparticles using liquid-cell transmission electron microscopy. *J. Am. Chem. Soc.* **2019**, *141*, 12601–12609. [[CrossRef](#)] [[PubMed](#)]
44. Song, M.; Zhou, G.; Lu, N.; Lee, J.; Nakouzi, E.; Wang, H.; Li, D. Oriented attachment induces fivefold twins by forming and decomposing high-energy grain boundaries. *Science* **2020**, *367*, 40–45. [[CrossRef](#)]
45. Jin, B.; Sushko, M.L.; Liu, Z.M.; Jin, C.H.; Tang, R.K. In situ liquid cell TEM reveals bridge-induced contact and fusion of Au nanocrystals in aqueous solution. *Nano Lett.* **2018**, *18*, 6551–6556. [[CrossRef](#)] [[PubMed](#)]
46. Li, J.J.; Wang, Z.C.; Deepak, F.L. In-situ atomic-scale observation of droplet coalescence driven nucleation and growth at liquid/solid interfaces. *ACS Nano* **2017**, *11*, 5590–5597. [[CrossRef](#)]
47. Keller, D.; Henninen, T.R.; Erni, R. Formation of gold nanoparticles in a free-standing ionic liquid triggered by heat and electron irradiation. *Micron* **2019**, *117*, 16–21. [[CrossRef](#)]
48. Browning, N.D.; Chisholm, M.F.; Pennycook, S.J. Atomic-resolution chemical analysis using a scanning transmission electron microscope. *Nature* **1993**, *366*, 143–146. [[CrossRef](#)]
49. Li, J.J.; Lv, S.H.; Chen, C.L.; Huang, S.M.; Wang, Z.C. Interfacial defect complex at the MgO/SrTiO<sub>3</sub> heterojunction and its electronic impact. *RSC Adv.* **2014**, *4*, 51002–51007. [[CrossRef](#)]
50. Chen, C.L.; Lv, S.H.; Li, J.J.; Wang, Z.C.; Liang, X.B.; Li, Y.X.; Viehland, D.; Nakajima, K.; Ikuhara, Y. Two-dimensional electron gas at the Ti-diffused BiFeO<sub>3</sub>/SrTiO<sub>3</sub> interface. *Appl. Phys. Lett.* **2015**, *107*, 031601. [[CrossRef](#)]

51. Barnard, A.S.; Young, N.P.; Kirkland, A.I.; Van Huis, M.A.; Xu, H.F. Nanogold: A quantitative phase map. *ACS Nano* **2009**, *3*, 1431–1436. [[CrossRef](#)] [[PubMed](#)]
52. Koga, K.; Ikeshoji, T.; Sugawara, K.-I. Size- and temperature-dependent structural transitions in gold nanoparticles. *Phys. Rev. Lett.* **2004**, *92*, 115507. [[CrossRef](#)] [[PubMed](#)]
53. Young, N.P.; Van Huis, M.A.; Zandbergen, H.W.; Xu, H.; Kirkland, A.I. Transformations of gold nanoparticles investigated using variable temperature high-resolution transmission electron microscopy. *Ultramicroscopy* **2010**, *110*, 506–516. [[CrossRef](#)] [[PubMed](#)]

**Disclaimer/Publisher’s Note:** The statements, opinions and data contained in all publications are solely those of the individual author(s) and contributor(s) and not of MDPI and/or the editor(s). MDPI and/or the editor(s) disclaim responsibility for any injury to people or property resulting from any ideas, methods, instructions or products referred to in the content.